Experiments in Fluids (2005) 38: 466–475
DOI 10.1007/s00348-004-0926-8

ORIGINALS

Atsuhide Kitagawa · Koichi Hishida · Yoshiaki Kodama

Flow structure of microbubble-laden turbulent channel flow measured by PIV combined with the shadow image technique

Received: 21 March 2004 / Revised: 11 November 2004 / Accepted: 19 December 2004 / Published online: 11 March 2005

Abstract The turbulence structure of a horizontal channel flow with microbubbles is experimentally investigated using combined particle image velocimetry (PIV) in order to clarify the mechanism of drag reduction caused by microbubbles. A new system which simultaneously measures the liquid phase and the dispersed bubbles is proposed, based on a combination of particle tracking velocimetry (PTV), laser-induced fluorescence (LIF) and the shadow image technique (SIT). To accurately obtain the velocity of the liquid phase, tracer particles which overlap with the bubble shadow images are almost entirely eliminated in the post-processing. Finally, the turbulence characteristics of the flow field are presented, including measurements for both phases, and the bubble effect on the turbulence is quantified.

Keywords Microbubble flow · Drag reduction · Turbulence modification · Particle tracking velocimetry (PTV)

1 Introduction

Frictional drag reduction has a large potential for improving the transport efficiency of ships, since as much as 80% of the total resistance is due to skin friction. A number of drag reduction devices have been proposed in the past, including riblets, large-eddy-break-up devices and micromachines, but none of them has been put to practical use so far.

McCormick and Bhattacharyya (1973) first showed that microbubbles, i.e. small air bubbles, injected into the turbulent boundary layer developing on a solid wall have a significant skin friction reduction effect. Madavan et al. (1984) injected air bubbles through a porous plate and demonstrated skin friction reduction of up to 80%. Kawakita and Takano (2000) injected bubbles through a plate with an array of small drilled holes, thus causing nominal pressure loss, and obtained a skin friction reduction comparable to that reported by Madavan et al. (1984).

Microbubbles are regarded to be particularly suited to large-box-shaped ships, such as tankers, because bubbles injected near the bow are expected to stay close to the bottom hull by buoyancy and efficiently cover the entire bottom surface. Kodama et al. (2000) carried out microbubble experiments by towing a 50-m-long flat plate in a 400-m-long towing tank at a speed of 7 m/s corresponding to 14 knots, a typical cruising speed of a large tanker, and found out that the skin friction reduction effect persists almost to the downstream end. Based on the measured total drag reduction, Kodama et al. (2002) estimated a 5% net power saving, taking into account the energy needed to inject bubbles, in the case where microbubbles were applied to a ship of 100 m in length and 7 m in water depth.

Recently, Nagamatsu et al. (2002) carried out a full-scale microbubble experiment using a 116-m-long training ship, and obtained a 3% total drag reduction and a 2% net power-saving, taking into account the hydrostatic pressure at the point of injection, at a speed of 14 knots. Fouling at sea greatly increases surface roughness and, consequently, increases skin friction. Deutsch et al. (2003) conducted microbubble experiments on rough surfaces and showed that the rate of

A. Kitagawa (✉)
Department of Mechanical and System Engineering,
Kyoto Institute of Technology, Goshokaido-cho,
Matsugasaki, Sakyou-ku, Kyoto 606-8585, Japan
E-mail: kitagawa@kit.ac. jp
Tel.: +81-75-724-7327
Fax: +81-75-724-7300

K. Hishida
Department of System Design Engineering,
Keio University, 3-14-1 Hiyoshi, Kohoku-ku,
Yokohama, Kanagawa 223-8522, Japan

Y. Kodama
Center for Smart Control of Turbulence,
National Maritime Research Institute,
6-38-1 Shinkawa, Mitaka, Tokyo 181-0004, Japan

skin friction reduction on rough surfaces is greater than that on smooth surfaces.

From these experiments, a marked improvement in the transport efficiency of ships using the microbubble technique is expected. This has prompted experiments and numerical simulations on bubble-laden turbulent flows. The turbulence properties of gas–liquid bubbly upward flows in a rectangular channel were experimentally studied by So et al. (2002) using laser Doppler velocimetry (LDV). They found that the mean liquid velocity near the wall becomes larger because of the driving force of buoyant bubbles, and that the streamwise turbulence intensity near the wall is enhanced. Minato et al. (2003) investigated turbulence modification in a bubbly pipe flow using a particle image velocimetry with laser-induced fluorescence (PIV/LIF) technique, revealing that the large number of bubbles near the wall disturb the transport of the turbulence energy produced in the wall shear layer.

On the other hand, Xu et al. (2002) simulated a turbulent boundary layer with microbubbles using a force-coupling method (FCM), and revealed that the drag reduction transiently occurs as the bubbles disperse from the wall due to the turbulence. Ferrante and Elghobashi (2004) performed a direct numerical simulation (DNS) on a spatially developing turbulent boundary layer laden with microbubbles. They discussed the physical mechanisms of the microbubble drag reduction, e.g. the displacement of the quasi-streamwise longitudinal vortical structures from the wall due to the presence of bubbles. However, the mechanism for drag reduction is still not fully understood. This is mainly because, in most experiments, information is lacking on bubble motion and the local interaction between bubbles and the surrounding liquid, and, in most simulations, simulated results are limited due to restrictions introduced by assumptions (e.g. the bubble is assumed to be spherical and rigid).

The objective in the present work is to experimentally study the mechanism of microbubble drag reduction using the combined PIV system. A number of aspects must be considered:

1. When conducting measurements of a microbubble flow using light sources of high intensity, such as laser light, the intensity of the light from tracer particles may be overwhelmed by light scattered at the bubble interface and from the walls, saturating the CCD camera. One of the ways to overcome this problem is to apply LIF to the measurements.
2. It is expected that turbulence modification in the microbubble flow depends strongly on the local interaction between bubbles and the surrounding liquid. This implies the necessity of simultaneous measurement of both phases.
3. The microbubble flow contains a large number of bubbles, whereby it is very difficult to accurately distinguish between the liquid and bubble velocities. As a consequence, we are apt to confuse the information on the velocities of both phases. This implies that the quality of the phase separation in the image directly affects the accuracy of the liquid velocity determination.

For these reasons, a new measurement system and a technique for liquid velocity detection with high accuracy are introduced in Sects. 2 and 3. The turbulence characteristics of the flow field in a horizontal channel with microbubbles are then presented and discussed in Sect. 4.

2 Experimental setup

2.1 Experimental apparatus and measurement method

Figure 1a shows a diagram of the experimental apparatus. The liquid circulates through the pump, the electro-magnetic flow meter, the channel (test section) and the dump tank. Air bubbles injected in the channel are removed in the dump tank by buoyancy, thus, allowing continuous operation. The channel is made of transparent acrylic resin with inner dimensions $H \times B \times L = 15 \times 100 \times 3{,}000$ mm. The gas injection device is set 1,028 mm downstream from the inlet nozzle. Air bubbles are injected into the channel through an array-of-holes plate (AHP) installed on the upper wall. The AHP has an injection area of $B_A \times L_A = 72 \times 36$ mm, where 0.25-mm-diameter holes are drilled at 3.5-mm spanwise and 5-mm streamwise intervals. The origin of the Cartesian coordinates (x streamwise, y wall-normal and z spanwise) is located at the centre of the air injection plate on the upper wall and the y axis is oriented upward. The test region is set at $x = 500$ mm and $z = 0$ mm.

In the present study, the velocity vectors of the liquid phase and dispersed bubbles are measured by an image processing technique. This technique is described in detail in Sect. 3. In addition, the LIF is applied in order to reduce optical problems, such as the light scattered at the bubble interface and the reflections generated at the wall of the channel. Fluorescent particles with Rhodamine-B as the fluorescent dye are applied as the tracer particles for the image processing technique. The specific density and the diameter of the particles are, respectively, 1.03 g/cm^3 and approximately 1–10 μm. The absorption wavelength region of the Rhodamine-B ranges from approximately 460 nm to 550 nm, and that of the emission from approximately 550 nm to 700 nm. The particle concentration in the measurement is approximately 60 ppm. Additionally, the shadow image technique (SIT), which was proposed by Tokuhiro et al. (1998), is applied for obtaining both the shape and the location of individual bubbles. In the SIT, each bubble image is obtained as a shadow.

Figure 1b shows an outline of the optical measurement system. This figure illustrates a cross-sectional view of the channel. In this system, two CCD cameras

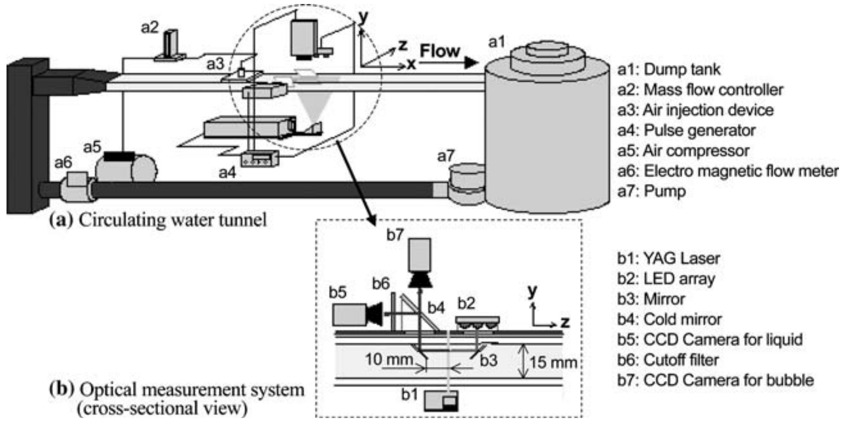

Fig. 1 Diagram of experimental apparatus

(Kodak ES1.0) are utilised for performing the measurement of both phases. The horizontal camera (b5) in this figure is used for the measurement of the liquid tracers while the vertical camera (b7) is used for the measurement of the bubbles. A Nd:YAG laser ($\lambda = 532$ nm) with a pulse intensity of 25 mJ and an LED array ($\lambda = 850$ nm) function as light sources for the measurement of each phase. The laser light sheet with a thickness of about 1.0 mm illuminates from the lower part of the channel at $z = 0$, while the infrared light traverses the upper part of the channel. The infrared light enters the channel through a mirror mounted on the upper wall. Scattered light is reflected upwards through a second mirror installed on the upper wall of the channel. Both mirrors are 15 mm in length, 9 mm in breadth and 1.5 mm in thickness. The angle between the mirrors and the upper wall is 45°. The gap distance between the mirrors is a minimum of 20 mm. To separate the visible and infrared light, a cold mirror (Sigmakoki CLDM-50S), which reflects the visible light and transmits the infrared light, is utilized. Furthermore, the images of the fluorescent particles are captured through a cutoff filter ($\lambda = 550$–720 nm; $T > 95\%$, $\lambda = 532$ nm; $T < 0.03\%$, $\lambda = 815$–885 nm; $T < 0.01\%$) to suppress the high intensity light reflected from the bubble interface.

The trigger timings of the laser, the LEDs and the two CCD cameras are synchronised using a pulse generator. The CCD images (1,008 × 1,018 pixels by 8-bit grey level) are acquired at a frame rate of 30 fps and are transferred to PCs. The field of view is 15.0 × 6.0 mm and the spatial resolution is 0.016 mm/pixel. The experimental conditions are shown in Table 1.

Table 1 Experimental conditions

Channel size	3,000 × 15 × 100 mm
Temperature of liquid	24.0–25.0°C
Kinematic viscosity of liquid	$\nu = 0.91 \times 10^{-6}$ m^2/s
Channel half height	$h = 7.5$ mm
Bulk liquid velocity	$U_m = 5.0$ m/s
Bulk Reynolds number	$Re_m = h \cdot U_m / \nu = 41{,}200$
Bulk void fraction	$\alpha = 0.5\%$
Mean bubble diameter	$D_a = 0.53$ mm

Tap water, from which contaminants have been removed by filtration, is used as the working fluid. The bulk velocity of the liquid U_m is 5 m/s. The bulk Reynolds number Re_m based on U_m and the channel half-height h is approximately 41,200. The mean bubble diameter D_a is approximately 0.53 mm. The void fraction α in this table is defined as:

$$\alpha = \frac{Q_G}{Q_G + Q_L}, \quad (1)$$

where Q_L and Q_G, respectively, stand for the liquid flow rate and the gas flow rate.

2.2 Effect of mirror on the flow field

In the present system, two mirrors are mounted inside the channel and it is unclear as to what their effect is on the flow structure. Therefore, the displacement thickness δ^* on the mirror and the fluctuation scale of the turbulence in the spanwise direction w' are roughly estimated. The displacement thickness δ^* is estimated to be:

$$\delta^* = 0.37 x_M \left(\frac{U_m x_M}{\nu} \right)^{-1/5}, \quad (2)$$

where U_m is the mean liquid velocity, x_M is the length of the mirror in the streamwise direction (= 15 mm) and ν is the kinematic viscosity of the liquid. Consequently, the displacement thickness δ^* at the end of the mirror is approximately 0.6 mm in the case of $U_m = 5.0$ m/s. In addition, the fluctuation scale in the spanwise direction w', which is estimated by DNS results for $Re = 13{,}800$ (Moser et al. 1999) is approximately 0.9 mm. These lengths are much smaller than the minimum separation distance between the mirror and the test region, which is approximately 10 mm. Additionally, the distance in which the two-point correlation of liquid fluctuation velocity in the spanwise direction reduces sufficiently is expected to be approximately 3 mm. Therefore, the effect of the mirrors on the flow field is considered to be negligible.

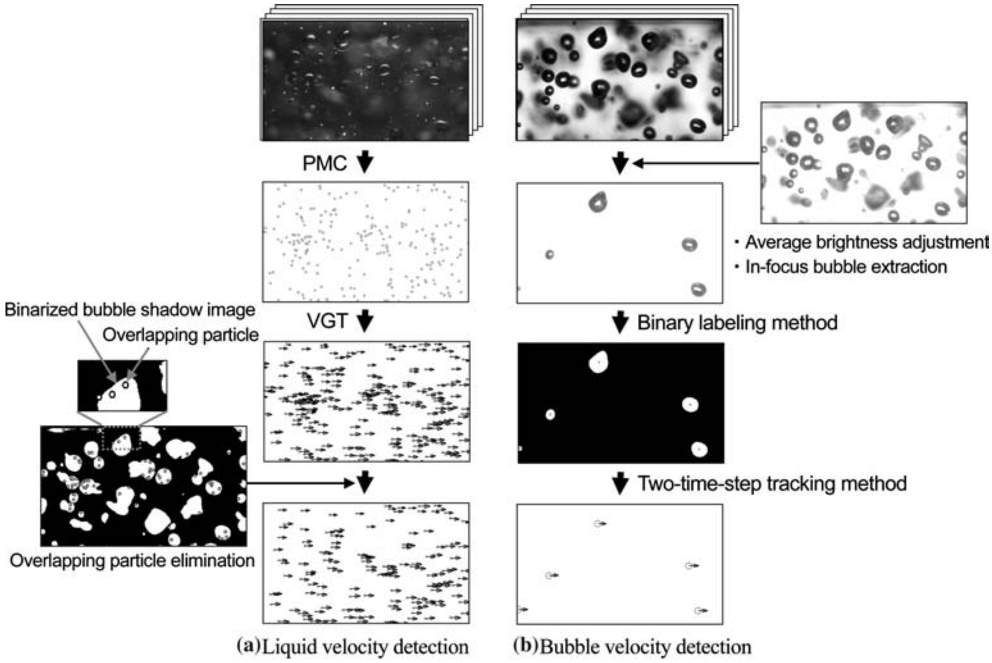

Fig. 2 Flow chart of the image processing for liquid and bubble velocity estimation

3 Measurement techniques

3.1 Technique for liquid phase velocity determination

One of the advantages of measurements using image processing is that simultaneous measurement of the two phases can easily be achieved by combining various processing techniques (e.g. Hassan et al. 2001; Lindken and Merzkirch 2002; Bröder and Sommerfeld 2002). For the measurement of liquid turbulent flow including a large number of bubbles, e.g. microbubble flow, the particle tracking velocimetry (PTV) technique is considered to be more suitable as an image processing technique compared to the PIV technique. This is because, with PIV, liquid velocity vectors of high accuracy cannot be estimated with increasing void fraction. This originates from the decrease of inter-bubble gaps in relation to the interrogation area dimensions and the increase of liquid fluctuation velocities induced in the bubble wake. For this reason, we measure the velocity of the liquid phase using the PTV technique. The procedures for measuring the liquid phase are as follows (see Fig. 2a):

1. By using the particle mask correlation (PMC) method proposed by Takehara and Etoh (1999), the centroid of each fluorescent tracer particle is calculated from the original images taken with the CCD camera. In this method, the particle mask, which is the brightness pattern of a particle image, is assumed to have the shape of the two-dimensional Gaussian distribution.
2. The velocity vectors of individual fluorescent tracer particles are calculated by the velocity gradient tensor (VGT) method with a time separation of 26 μs between pairs of images. This particle tracking algorithm, developed by Ishikawa et al. (2000), uses a velocity gradient tensor to take the deformation ratio of fluid flows into account. They showed that, in flow fields having high wavelength rotational motions, this algorithm has a higher correct capturing ratio than other PTV algorithms, such as the binary image cross-correlation method (e.g. Yamamoto et al. 1996) and the four-time-step tracking method (e.g. Nishino et al. 1989).

We suspect that some velocity vectors in the vicinity of the bubble interface are erroneous because the flow field in the present study is turbulent with a local high bubble density. Therefore, the velocity vector of any tracer particle which deviates more than three standard deviations from the mean velocity is regarded as an incorrect vector and is removed from subsequent proceedings. The validity of the definition of an incorrect vector will be discussed in Sect. 4.4. Regarding the mean velocity and the turbulence intensity of the liquid in the streamwise direction, the relative errors of the present data to previously obtained LDV measurements are, at most, approximately 2.5% and 4.0%, respectively.

3.2 Technique for bubble velocity detection

Several techniques for calculating the centroids of bubbles have been proposed; for instance, a binary labelling method (e.g. Yamamoto et al. 1996) and a template matching method (e.g. van der Brug 1977). The binary labelling method can treat the deformation of a bubble but it cannot treat overlapping bubbles. In contrast, the template matching method can treat the latter, but not the former. In the present study, the binary labelling method is adopted due to the reduced computational load, although in microbubble flows, a large number of bubbles overlap. Consequently, in-focus overlapping bubbles are not considered. The procedure for measuring the bubbles is as follows (see Fig. 2b):

1. The average brightness of the original images obtained by the SIT is adjusted to emphasise the edges of the bubbles and to remove the noise, and then only in-focus bubbles are extracted.
2. The brightness of the images is inverted to simplify the handling of the process given below. The centroids of the bubbles are then calculated from the images, which are binarised using the method proposed by Otsu (1979). In this method, a threshold is determined from the histogram of the brightness in the image.
3. The velocity vectors of the bubbles are simply calculated from bubble positions in two frames because, in most cases, the displacement of the bubbles per frame is smaller than the bubble radius.

In this study, the bubble diameter is calculated as the equivalent of the constituent pixel number of individual bubbles. The equivalent diameter D of individual bubbles ranges from 10 pixels to 60 pixels. The displacement of the centroids of the bubbles is 7–13 pixels per frame. According to our analysis with artificial images for the bubbles, the error of the displacement of the centroid of the bubble is around 0.1 pixels for $D = 10$ pixels. Consequently, it is estimated that the uncertainty in the bubble velocity vector determined by the detection of the centroid of the bubbles is within approximately 2.9%.

3.3 Elimination of the tracer particle overlapping the bubble shadow image

The treatment of tracer particles overlapping the bubble shadow images is one of the essential issues for the detection of the liquid velocity in microbubble flows. For the sake of convenience, such a tracer particle is, hereinafter, called an overlapping particle. For instance, the velocity of the bubble interface is detected by the PTV technique when the fluorescent tracer particle attaches itself to the bubble. Furthermore, an erroneous fluctuation velocity is detected when bubbles exist between the camera and the measurement plane because the fluorescent light from tracer particles can be refracted at the bubble interface. In this paper, a procedure for eliminating the overlapping particles is introduced in order to detect the liquid velocity with high accuracy. Such elimination of overlapping particles is not possible in the process mentioned in Sect. 3.1 because, in most cases, the fluctuation velocities of the overlapping particles are smaller than that estimated from the incorrect vectors. The procedure of the elimination method is as follows: (1) the original images obtained by the SIT are binarised, i.e. the binary value is 1 for bubble and 0 for non-bubble; (2) the tracer particle positions obtained by the PMC method are collated with the binary data (see Fig. 2a). When the binary value at the tracer particle position is 1, it is defined as the overlapping particle and is then eliminated.

4 Results and discussions

4.1 Skin friction coefficient

Figure 3 shows the skin friction coefficient measured at the upper wall at $U_m = 5.0$ m/s, where the test position is set at $x = 500$ mm and 1,000 mm. In this figure, the horizontal axis is the bulk void fraction while the vertical axis is the ratio of the skin friction coefficient in the bubbly flow C_f to that in the single-phase flow C_{f0}. The skin friction coefficient C_{f0} is given by:

$$C_{f0}(Q_G) = C_{f0}(0)\frac{\tau[U(Q_G)]}{\tau[U(0)]}, \quad (3)$$

where $U(Q_G)$ is the mean liquid velocity at Q_G and τ is the wall shear stress and is estimated by the empirical Blasius formula for turbulent pipe flow (Schlichting 1979), taking the hydraulic radius into account. That is, C_{f0} is corrected for the blockage effect as a function of the gas flow rate (see Kodama et al. 2000). It is seen that the ratio of the skin friction coefficient reduces with increasing void fraction. It is also seen that the drag reduction effect is approximately 2.5% when the void fraction is 0.5%, which is the experimental condition for which detailed velocity measurements were performed.

4.2 Distribution of local bubble shadow area fraction

To estimate the pattern of bubble distribution in the microbubble flow, the local shadow area fraction of the bubble is calculated using the binarised images of the bubbles. Figure 4 shows the distribution of the local

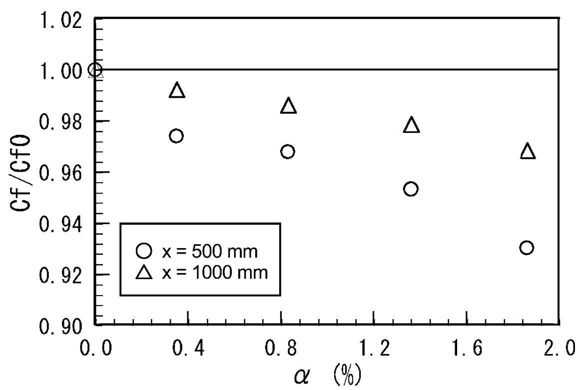

Fig. 3 Ratio of skin friction coefficient in bubbly flow to that in single-phase flow at $U_m = 5.0$ m/s

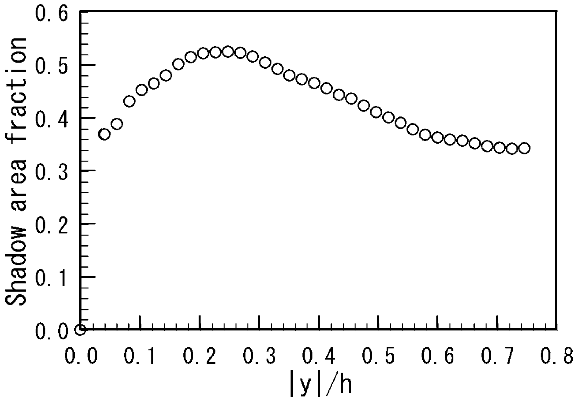

Fig. 4 Distribution of local bubble shadow area fraction

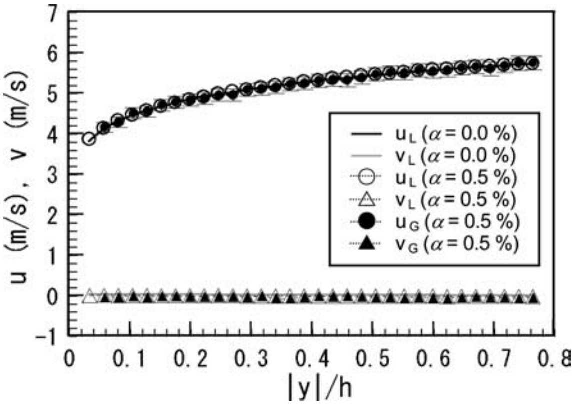

Fig. 6 Mean velocity profile of liquid phase and bubbles

bubble shadow area fraction at $\alpha = 0.5\%$. The horizontal axis is the distance from the upper wall of the channel normalised by the channel half-height h. It is clear that the peak in the bubble shadow area fraction is not located near the wall but instead at $|y|/h = 0.2 - 0.3$. This is larger than the typical dimensionless mean bubble diameter $D_a/h = 0.07$.

4.3 Simultaneous measurement data obtained by the PTV/LIF/SIT system

Figure 5 indicates a typical measured result for one image frame taken at $\alpha = 0.5\%$. In this figure, the grey and black regions are, respectively, the out-of-focus and the in-focus bubble shadow images obtained by the SIT. The arrows stand for the liquid velocity and the velocity of the in-focus bubbles. The upper part of the image corresponds to the upper wall of the channel. It is observed that liquid velocity vectors around individual bubbles and the velocity vectors of in-focus bubbles can be obtained relatively well. In addition, no overlapping particles which induce the erroneous fluctuation velocity can be observed. With the proposed PTV/LIF/SIT system, it is, therefore, possible to simultaneously measure both the liquid phase and the dispersed bubbles, and the estimated turbulence statistics are provided below as reliable data.

4.4 Microbubble flow characteristics

To obtain detailed information on turbulence structures in the microbubble flow, statistical analysis of the data for both the liquid phase and the bubble is performed. The measurement plane has been divided into 32 segments in each direction and the grid spacing is approximately 0.176 mm. The number of samples for the liquid phase statistics is more than 5,000 in each grid element. Regarding the bubbles, only estimates based on more than 200 samples per grid element are indicated.

Figure 6 shows the mean velocity profile of the liquid phase and bubbles. In this figure, u and v represent the mean velocities in the streamwise and wall-normal directions, and the subscript L and G are, respectively, the liquid phase and the bubble. It is seen that the streamwise mean liquid velocity is almost unchanged by the bubble injection. This suggests that, under the present experimental conditions, the change in the viscous shear stress accompanied by bubble injection is negligible. It is also seen that the vertical mean liquid

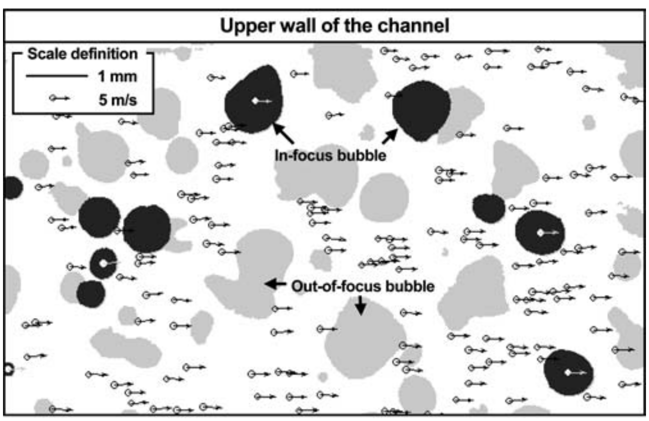

Fig. 5 PTV/LIF/SIT result at $\alpha = 0.5\%$

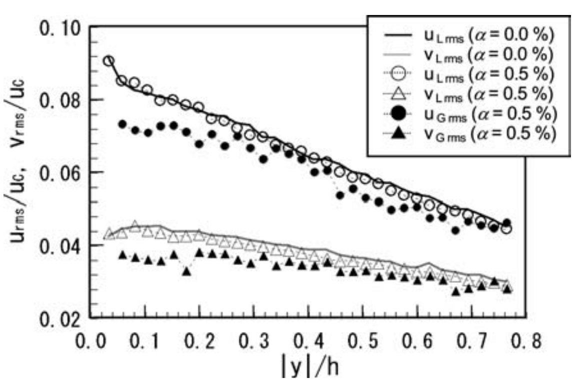

Fig. 7 Turbulence intensity profile of liquid phase and bubble

velocity is zero across the channel. The reflection generated at the wall of the channel, which has been a problem for the measurement of microbubble flow using the image processing technique, is, therefore, negligible. Moreover, it is clear that the liquid velocity profile is almost the same as the bubble velocity profile.

Figure 7 shows the turbulence intensity profile of the liquid phase and the bubble, which is normalised by u_C. Here, u_C is the maximum velocity of the single liquid phase at the centre of the channel ($y=h$) and is approximately 5.82 m/s. In this figure, u_{rms} and v_{rms}, respectively, represent the standard deviations of the streamwise and wall-normal velocity components. It is clear that the liquid turbulence intensity in the streamwise direction decreases slightly in a few regions, while that in the wall-normal direction decreases slightly in the whole of the region, as a result of the bubble injection. It is also clear that the difference in the turbulence intensities between the liquid phase and the bubble becomes larger as the normalised distance from the wall becomes smaller. It is expected that this results from the fact that, in the vicinity of the wall, liquid motion on a small scale does not have a significant effect on bubble motion. Moreover, it is seen that the bubble turbulence intensities are smaller than the liquid turbulence intensities. This confirms the validity of the definition of an incorrect vector mentioned in Sect. 3.3 because the possibility of increased liquid fluctuation velocities around bubbles is quite low.

Figure 8 shows the profiles of the Reynolds stress of the liquid phase and the correlation of the bubble fluctuation velocities, which are normalized by $u_C{}^2$. It is obvious from this figure that the Reynolds stress is decreased in the whole region by injecting bubbles. This shows a similar tendency to that of previous data proposed by Hassan et al. (2004) and this reduction ratio of the Reynolds stress is roughly the same as that of the skin friction coefficient shown in Fig. 3. It is also obvious that the correlation of the bubble fluctuation velocities is much smaller than the Reynolds stress of the liquid phase. This originates mainly from the timescale of the bubble motion being much larger than that of the surrounding liquid turbulence motion. We will discuss the mechanism of the Reynolds stress reduction in the next section.

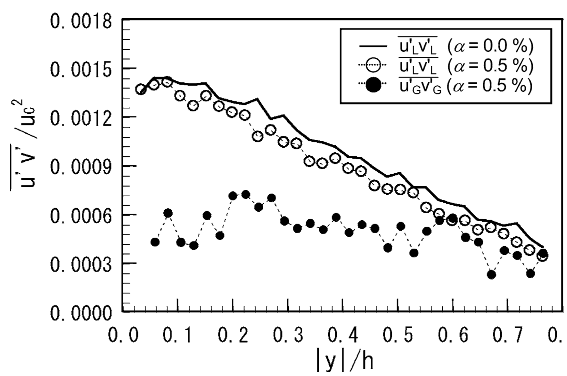

Fig. 8 Profiles of Reynolds stress of the liquid phase and correlation of bubble fluctuation velocities

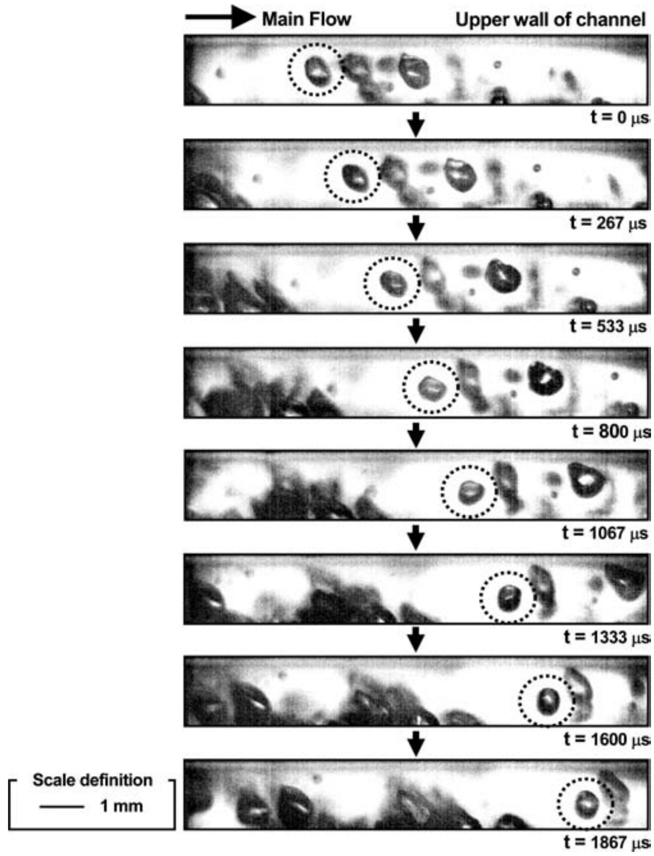

Fig. 9 Bubble motion in the vicinity of the upper wall of the channel

4.5 Bubble deformation effect

In this section, the bubble deformation effect on the turbulence modification around the bubble is investigated to clarify the mechanism of the decrease in the Reynolds stress. The images in Fig. 9 show the consecutive images of an in-focus bubble in the vicinity of the upper wall of the channel, which was taken with a high-speed camera (IDT, X Stream XS-3, resolution: 1,024 × 640 pixels). The shutter speed of the camera is 1/50,000 s and the frame rate is 3,750 fps. From this figure, it is clearly observed that the degree of deformation and the inclination angle of the bubble vary significantly as time elapses. Figures 10 and 11, respectively, show the relationship between the bubble equivalent diameter D and the bubble inclination angle θ to the bubble deformation ratio γ, which is defined as:

$$\gamma = \frac{L-D}{D}. \quad (4)$$

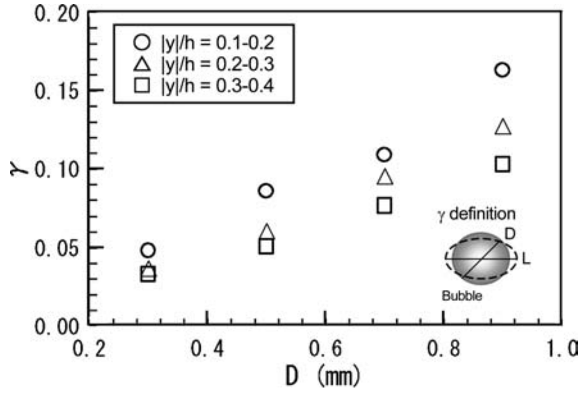

Fig. 10 Relationship between bubble diameter and bubble deformation ratio

L is the length of the longer axis of the bubble, assuming an ellipsoidal shape. The schematic definitions of θ and γ are illustrated in each figure. θ is set to be positive on the upper wall side. Each data point is an averaged value over the bubbles inside each region, i.e. $|y|/h = 0.1 - 0.2$, 0.2–0.3 and 0.3–0.4. It is clear from Fig. 10 that γ becomes large as D increases and the distance from the upper wall decreases. From Fig. 11, it is clear that γ varies with θ and that in all $|y|/h$ regions, γ is the largest when θ ranges from $-60°$ to $-30°$.

To make clear the turbulence modification due to local liquid–bubble interaction, the frequency of occurrence of negative $u'_L v'_L$, η, is calculated. The domain for detecting the $u'_L v'_L$ in proximity to the in-focus bubble is defined in Fig. 12a, in which La is the half-length of L. Xa and Ya are, respectively, the lengths of the domain in the streamwise and the wall-normal directions, and Ya is set to La. η is defined as N_I / N_T, where N_I is the detection number of the negative $u'_L v'_L$ around the in-focus bubble and N_T is the sampling number (see Fig. 12b). Note that, in the case of the present co-ordinate system, the Reynolds stress on the upper wall side decreases with increasing η.

Figure 13 shows the calculated frequency averaged at $|y|/h = 0.1 - 0.2$, 0.2–0.3 and 0.3–0.4. The "infinity" in this figure means that $X\text{a} \to \infty$. It is clear that, in all $|y|/h$ regions, η increases with decreasing Xa. This indicates that the turbulence around the bubble has a tendency to become isotropic. It is, therefore, expected that the increase in the bubble number density makes the turbulence isotropic over a wide range. This corresponds to the previous measurement showing that the frictional drag reduces with increasing void fraction. Figure 14 indicates the relationship between the bubble deformation ratio γ and the frequency of occurrence of negative $u'_L v'_L$, η, at $X\text{a} = 4L\text{a}$ and $Y\text{a} = L\text{a}$. From this figure, it is obvious that, in all $|y|/h$ regions, η increases as γ is increased. According to our analysis, this tendency is

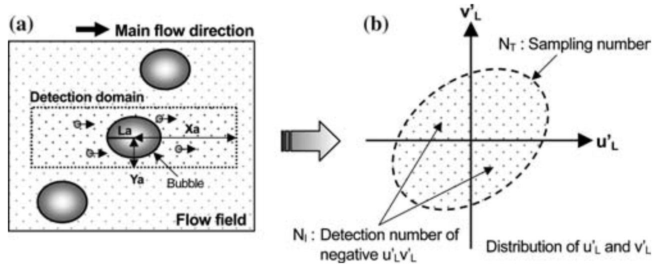

Fig. 12 Schematic explanation for calculating the frequency of the occurrence of negative $u'_L v'_L$

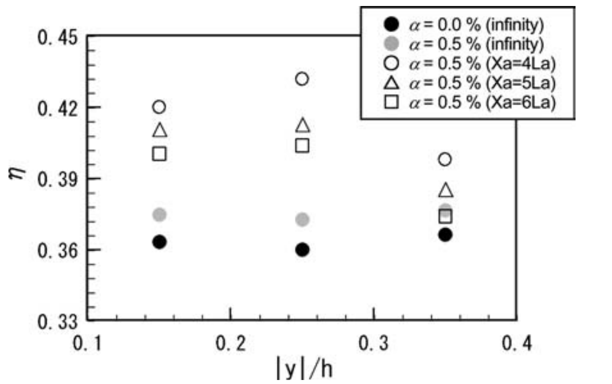

Fig. 13 Frequency of the occurrence of negative $u'_L v'_L$ at $Y\text{a} = L\text{a}$

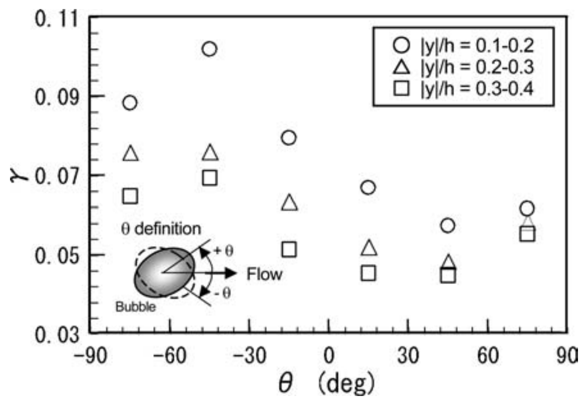

Fig. 11 Relationship between bubble inclination angle and bubble deformation ratio

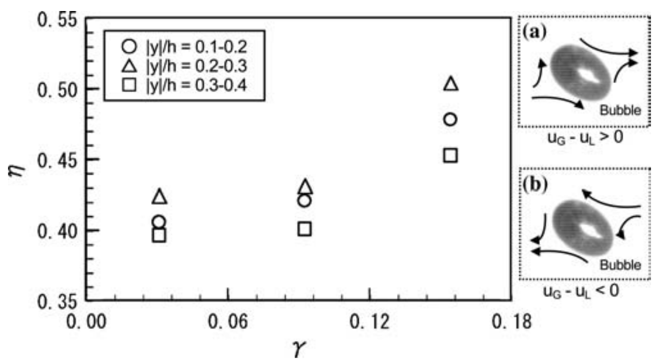

Fig. 14 Relationship between bubble deformation ratio and frequency of the occurrence of negative $u'_L v'_L$ at $X\text{a} = 4L\text{a}$ and $Y\text{a} = L\text{a}$

also seen in other conditions, e.g. $4La < Xa < 6La$ and $0.8La < Ya < 1.2La$. This means that the bubble deformation contributes to the isotropy of the turbulence, which causes the decrease in the Reynolds stress. The reason for the decrease in the Reynolds stress due to the bubble deformation is explained as follows. The longer axis of the bubble with large deformation tends to be in parallel with the axis of the distortion of the mean liquid velocity, as shown in Fig. 11, Under this situation, the liquid in proximity to the deformed bubble is in the same direction as the longer axis because it currents along the bubble interface, whether the relative velocity between the surrounding liquid and the bubble is positive or not (see Fig. 14a, b). Consequently, the correlation between u'_L and v'_L around a bubble with an inclination angle ranging from −30° to −60° is consistently negative. The generated negative $u'_L v'_L$ contributes directly to the isotropy of the turbulence. Note that the $u'_L v'_L$ around the bubble becomes positive when θ ranges from 30° to 60°, however, the frequency and the deformation ratio of its bubble are quite low (see Fig. 11) and its effect is barely noticeable.

From the above results, it was found that the decrease in the Reynolds stress is related to bubble deformation. In the future, we expect to carry out a detailed investigation into the bubble deformation effect to comprehensively clarify the mechanism of the frictional drag reduction due to microbubbles.

5 Conclusions

The turbulence structure of microbubble flow in a horizontal channel was investigated experimentally using an image processing technique in order to clarify the mechanism of the drag reduction caused by microbubbles. Under the condition that the bulk void fraction is approximately 0.5%, the following conclusions can be drawn from the present study:

1. A new simultaneous measurement system based on the combination of particle tracking velocimetry, laser induced fluorescence and the shadow image technique (PTV/LIF/SIT) was proposed and the velocity vectors of the liquid phase and bubbles were successfully detected. In addition, the fluorescent tracer particles overlapping the bubble shadow images were almost entirely eliminated in order to accurately detect the liquid velocity vectors.
2. The mean liquid velocity is almost the same as the mean bubble velocity.
3. By the injection of bubbles, the liquid turbulence intensity in the streamwise direction is decreased slightly in a few regions while that in the wall-normal direction decreases slightly in the whole of the region. In addition, the difference in the turbulence intensities between the liquid phase and the bubble becomes large as the normalised distance from the wall is decreased.
4. The Reynolds stress of the liquid is decreased in the whole region by injecting bubbles. This relates directly to the frictional drag reduction. The correlation of the bubble fluctuation velocities is much smaller than the Reynolds stress of the liquid phase.
5. The decrease in the Reynolds stress in the microbubble flow results from the negative $u'v'$ generated by the bubble deformation.

Acknowledgements This work was carried out as a research activity at the Center for Smart Control of Turbulence funded by the Ministry of Education, Culture, Sports, Science and Technology, Japan. We would also like to thank Dr. Sugiyama at the National Maritime Research Institute and Dr. Fujiwara at the University of Tokyo for their comments on this paper.

References

Bröder D, Sommerfeld M (2002) An advanced LIF–PLV system for analysing the hydrodynamics in a laboratory bubble column at higher void fractions. Exp Fluids 33:826–837

Deutsch S, Moeny M, Fontaine A, Petrie H (2003) Microbubble drag reduction in rough walled turbulent boundary layers. In: Proceedings of the 4th ASME/JSME joint fluids engineering conference and FED summer meeting and exposition CD-ROM, Kauai, Hawaii, July 2003, paper no. FEDSM2003-45647, pp 1–9

Ferrante A, Elghobashi S (2004) On the physical mechanisms of drag reduction in a spatially developing turbulent boundary layer laden with microbubbles. J Fluid Mech 503:345–355

Hassan YA, Ortiz-Villafuerte J, Schmidl WD (2001) Three-dimensional measurements of single bubble dynamics in a small diameter pipe using stereoscopic particle image velocimetry. Int J Multiphase Flow 27:817–842

Hassan YA, Gutierrez TCC, Jimenez BJA, Dominguez OE (2004) Vortical structure modification by microbubble injection in a channel flow. In: Proceedings of the 5th international conference on multiphase flow (ICMF 2004) CD-ROM, Yokohama, Japan, May/June 2004, paper no. 367, pp 1–8

Ishikawa M, Murai Y, Wada A, Iguchi M, Okamoto K, Yamamoto F (2000) Novel algorithm for particle tracking velocimetry using the velocity gradient tensor. Exp Fluids 29(6):519–531

Kawakita C, Takano S (2000) Microbubble skin friction reduction under the influence of pressure gradients and curved surface (in Japanese). J Soc Naval Archit Jap 188:11–21

Kodama Y, Kakugawa A, Takahashi T, Kawashima H (2000) Experimental study on microbubbles and their applicability to ships for skin friction reduction. Int J Heat and Fluid Flow 21:582–588

Kodama Y, Kakugawa A, Takahashi T, Nagaya S, Sugiyama K SR239 Committee (2002) Microbubbles: drag reduction mechanism and applicability to ships. In: Proceedings of the 24th symposium on naval hydrodynamics, Fukuoka, Japan, July 2002, pp 1–20

Lindken R, Merzkirch W (2002) A novel PIV technique for measurements in multiphase flows and its application to two-phase bubbly flows. Exp Fluids 33:814–825

Madavan NK, Deutsch S, Merkle CL (1984) Reduction of turbulent skin friction by microbubbles. Phys Fluids 27:356–363

McCormick ME, Bhattacharyya R (1973) Drag reduction of a submersible hull by electrolysis. Nav Eng J 85:11–16

Minato D, Tanaka T, Fujiwara A, Hishida K, Maeda M (2003) Particle tracking velocimetry measurement of bubble–bubble interaction. In: Proceedings of the 4th ASME/JSME joint fluids engineering conference and FED summer meeting and exposition CD-ROM, Kauai, Hawaii, July 2003, paper no. TED-AJ03–198

Moriguchi Y, Kato H (2002) Influence of microbubble diameter and distribution on frictional resistance reduction. J Mar Sci Technol 7: 79–85

Moser RD, Kim J, Mansour NN (1999) Direct numerical simulation of turbulent channel flow up to $Re_{\tau} = 590$. Phys Fluids 11(4):943–945

Nagamatsu T, Kodama Y, Kakugawa A, Takai M, Murakami K, Ishikawa S, Kamiirisa H, Ogiwara S, Yoshida Y, Suzuki T, Toda Y, Kato H, Ikemoto A, Yamatani S, Imo S, Yamashita K (2002) A full-scale experiment on microbubbles for skin friction reduction using SEIUN MARU part 2: the full-scale experiment (in Japanese). J Soc Naval Archit Jap 192:15–28

Nishino K, Kasagi N, Hirata M (1989) Three dimensional particle tracking velocimetry based on automatic digital image processing. ASME J Fluid Eng 111:384–391

Otsu N (1979) A threshold selection method from gray-level histograms. IEEE Trans Syst Man Cybern SMC 9(1):62–66

Schlichting H (1979) Boundary layer theory 7th ed. McGraw-Hill, New York

So S, Morikita H, Takagi S, Matsumoto Y (2002) Laser Doppler velocimetry measurement of turbulent bubbly channel flow. Exp Fluids 33:135–142

Takehara K, Etoh T (1999) A study on particle identification in PTV. J Visualization 1(3):313–323

Tokuhiro A, Maekawa M, Iizuka K, Hishida K, Maeda M (1998) Turbulent flow past a bubble and an ellipsoid using shadow–image and PIV techniques. Int J Multiphase Flow 24:1383–1406

van der Brug GJ (1977) Experiments in iterative enhancement of linear features. Comput Graph Image Processing 6:25–42

Xu J, Maxey MR, Karniadakis GE (2002) Numerical simulation of turbulent drag reduction using micro-bubbles. J Fluid Mech 468:271–281

Yamamoto F, Wada A, Iguchi M, Ishikawa M (1996) Discussion of the cross-correlation methods for PIV. J Flow Visual Image Processing 3(1):65–78